Available online at www.sciencedirect.com

ScienceDirect

Advances in Space Research 58 (2016) 821–834

ADVANCES IN SPACE RESEARCH (a COSPAR publication)

www.elsevier.com/locate/asr

Tucumán ionospheric model (TIM): Initial results for STEC predictions

L.A. Scidá [a,b,*], R.G. Ezquer [a,b,c], M.A. Cabrera [b,d], C. Jadur [e], A.M. Sfer [f]

[a] Laboratorio de Ionósfera, Dpto. de Física, FACET, Universidad Nacional de Tucumán, Av. Independencia 1800, CP4000 Tucumán, Argentina
[b] CIASUR, Facultad Regional Tucumán, Universidad Tecnológica Nacional, Tucumán, Argentina
[c] Consejo Nacional de Investigaciones Científicas y Tecnológicas, CONICET, Argentina
[d] Laboratorio de Telecomunicaciones, Dpto. de Electricidad, Electrónica y Computación, FACET, Universidad Nacional de Tucumán, Av. Independencia 1800, CP4000 Tucumán, Argentina
[e] Departamento de Matemática, Universidad Nacional de Salta, Salta, Argentina
[f] Departamento de Matemática, Universidad Nacional de Tucumán, Av. Independencia 1800, CP4000 Tucumán, Argentina

Received 23 October 2015; received in revised form 11 April 2016; accepted 5 May 2016
Available online 26 May 2016

Abstract

Most ionospheric models can calculate vertical total electron content (VTEC) predictions, but only a few are suitable for calculating slant total electron content (STEC). This ionospheric magnitude is generally measured for electron content determinations, with VTEC particularly corresponding to an elevation of 90°. This is generally obtained by applying a mapping function to STEC measurements, which leads to important calculation errors. Moreover, the equatorial region has unique characteristics, such as the fountain effect and the equatorial electrojet, which lead to significant errors in the model's calculations. In this paper, the Tucumán ionospheric model (TIM) is presented as a novel alternative for calculating the STEC in low-latitude regions (−24 to 24 dip latitude). The model is based on spatial geometry where the considered trajectory is segmented, and the corresponding electron density calculations for the resulting segment end points are determined using the semi-empirical low-latitude ionospheric model (SLIM) with reference to their corresponding magnetic coordinates and height. Finally, the electron density values are integrated along the path to obtain the STEC. This work describes the TIM and tests their STEC predictions for five ray paths around the world (totaling 16 cases under study), which are compared with experimental data from satellites and with those calculated by the NeQuick model. Moreover, the TIM performance for VTEC predictions is also checked and compared with VTEC data obtained from Global Positioning System (GPS) signals, IRI model, and NeQuick model predictions, for six GPS receiver stations during the equinox and solstice (totaling 12 cases studied). Comparisons of the TIM predictions with experimental data show that 53% of the calculation has, in general, deviations <30%. For the considered cases, TIM reproduces the experimental data better than the other models.

Keywords: STEC; VTEC; Equatorial anomaly; GPS; Electron density; Low-latitude ionosphere

1. Introduction

The effect of ionospheric plasma on the propagation of electromagnetic (EM) waves depends on the number of free electrons found in the propagation path of the wave. This is well represented by the slant total electron content (STEC), which is the number of free electrons in a cylinder of 1-m^2 cross section extending from the ground to the top of the ionosphere along the ray path. The interaction of

* Corresponding author at: Laboratorio de Ionósfera, Dpto. de Física, FACET, Universidad Nacional de Tucumán, Av. Independencia 1800, CP4000 Tucumán, Argentina.
E-mail addresses: lscida@herrera.unt.edu.ar (L.A. Scidá), rezquer@herrera.unt.edu.ar (R.G. Ezquer), mcabrera@herrera.unt.edu.ar (M.A. Cabrera), jadur@unsa.edu.ar (C. Jadur), asfer@herrera.unt.edu.ar (A.M. Sfer).

http://dx.doi.org/10.1016/j.asr.2016.05.005
0273-1177/

free electrons with EM waves has been widely studied and modeled (Komjathy, 1997; Abdu, 2005; Bilitza and Reinisch, 2008; Migoye Orue et al., 2015, among others). Although the ionosphere is hundreds of kilometers thick, with a height of around 50–2000 km, most of the free electrons are concentrated in a thin layer (≈100 km thick) centered approximately 400 km above the earth's surface (Hanbaba and Zolesi, 2000). Accordingly, attempts to model the TEC are usually based on a simplified version of a 2-D homogeneous ionosphere surrounding the earth at some specific radius (Smith et al., 2008). The use of such a model in the presence of important vertical and horizontal structures leads to significant TEC calculation errors. The action of the dynamo zonal electric field in the equatorial and low-latitude ionosphere causes a vertical plasma drift derived in electron density gradients, which lead to the main errors in the 2-D layer model.

1.1. The equatorial ionospheric anomaly

The Chapman theory describes the ionosphere (Chapman, 1931) as cold plasma where the ionization is controlled by the intensity of solar radiation and zenith angle. Any ionospheric phenomena that cannot be explained by the Chapman theory are called "anomalies." Early studies of these anomalies were conducted by Berkner et al. (1936). At low-latitude and equatorial regions, the most remarkable phenomenon is the well-known equatorial ionization anomaly (EIA) or equatorial anomaly (EA). The EIA is characterized by the occurrence of a throat in the ionization concentration at the equator, which crests at about 15° in magnetic latitude (Appleton, 1946) in each hemisphere. The EA has been described as arising from the electrodynamics at the equator. Martyn (1947) and Duncan (1960) proposed a theory based on EM drift. This theory assumes the existence of a daytime eastward electric field in the equatorial region, resulting in an upward vertical plasma drift. This electric field is established perpendicular to the magnetic field, and the ionization vertically drifts upward during the day and downward at night with a velocity of $\mathbf{E} \times \mathbf{B}/B^2$. The upward motion of ionization during the day is termed as the equatorial fountain, as ionization rises above the magnetic equator until pressure forces become appreciable. As a result, the ionization slows down, moves along the field lines under the force of gravity, and is deposited at higher tropical altitudes. The resulting ionization enhancement at tropical latitudes and a throat in ionization concentration at the magnetic equator is termed as the EIA.

1.2. The 2-D ionospheric shell model

Many attempts to model the ionospheric TEC have begun with the assumption that the ionosphere is a two-dimensional (2-D) layer surrounding the earth at some specific radius. The impact of using such a model and the presence of vertical and horizontal gradients lead to nonnegligible calculation errors (Smith et al., 2008).

The most common techniques for TEC determination are based on the phenomenon of Faraday rotation, the Doppler effect, and the time delay of two frequencies from geostationary satellites (GSATs), global navigation satellite systems (GNSSs) such as Global Positioning System (GPS) and GLONASS constellation, and each one has its peculiarities (Ezquer, 1990; Warnant and Jodogne, 1998; Gulyaeva, 1999; Reinisch, 2000; Panda et al., 2015; Cesaroni et al., 2015).

In general, the total electron content, the *STEC*, is defined as follows:

$$STEC = \int_{hbase}^{htop} N_e \cdot ds \tag{1}$$

In this equation, h_{base} (≈50 km) and h_{top} (≈2000 km) are the ray path boundaries, N_e is the electron density (assumed constant throughout the thickness of the layer), and ds is the differential distance traveled by the wave. *STEC* is expressed in m^{-2}, but the most common unit used is the TECU equivalent to $10^{16}\ m^{-2}$. The vertical total electron content (*VTEC*) is a particular case of *STEC*, where the signal travels through the ionosphere along the earth's radial direction, and it can be calculated from *STEC* via the mapping function.

The most common mapping function used seems to be the trigonometric function:

$$VTEC = STEC \cdot \cos z' \tag{2}$$

The z' angle is formed by the beam and the normal to the earth's direction, which are intercepted on a point of the shell (≈400-km height).This point is usually called the *ionospheric pierce point (IPP)* defined as "*the point where the line of sight between the satellite and the ground receiver intersects the shell layer.*" The geometry and other details of this subject are shown in Fig. 1.

The most obvious error associated with this mapping function is due to the representation of the ionosphere as a thin shell at the pierce point. Further, the simple mapping function used in Eq. (2) fails to address the curvature of the actual ionosphere, which leads to a second systematic

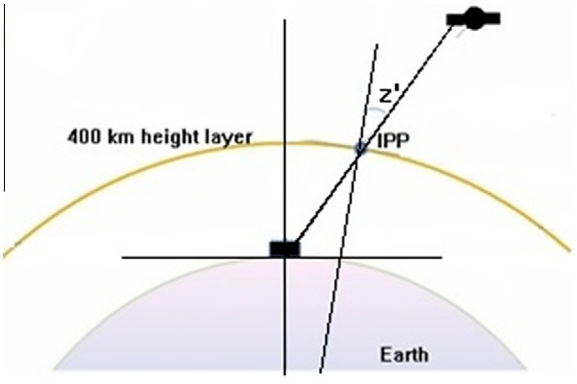

Fig. 1. Ionospheric shell layer geometry for TEC calculation.

error, from a purely geometric standpoint. Such errors can reach as high as 14% on days of no strong ionosphere activity. In the low-latitude and equatorial ionosphere, we can expect a significant increase in these errors due to horizontal gradients in the electron density (Cabrera, 2003; Smith et al., 2008, among others). Das Gupta et al. (2002) found some evidence on the errors produced when a simple mapping function is used in the EIA region.

1.3. The SLIM model

The semi-empirical low-latitude ionospheric model (SLIM) (Anderson et al., 1985) takes into account the vertical plasma drift caused by $\mathbf{E} \times \mathbf{B}$ Lorentz forces in low-latitude regions, which appreciably thickens both the base profile and the top, consequently leading to higher values of TEC (Namara, 1984). However, the calculations of the theoretical electron density profiles require considerable processing time even in a modern computer. Another alternative is theoretically calculating the electron density as a function of latitude and local time and then generating coefficients that reproduce these profiles. These coefficients are tabulated and stored and can be used to quickly generate more accurate electron density profiles for the low-latitude F region. This last concept was used in the SLIM formulation in order to finally calculate VTEC.

We can summarize the main features of the SLIM model as follows:

(i) The changes in electron density caused by the vertical $\mathbf{E} \times \mathbf{B}$ drift is incorporated in the Chapman model.
(ii) The enhancement in electron density due to the vertical $\mathbf{E} \times \mathbf{B}$ drift contribution boosts the base and top electron density profiles; consequently, the calculated TEC is greater.
(iii) The SLIM model calculates the electron density as a function of height and local time, by numerically solving the time-dependent continuity equation of the ion O+, as follows:

$$\frac{\partial N_i}{\partial t} + \nabla(N_i V_i) = P_i - L_i \tag{3}$$

where N_i: O^+ numerical density; P_i: O^+ production rate; L_i: O^+ loss rate; V_i: O^+ transport velocity.

When the coordinates are transformed to a system parallel and perpendicular to the geomagnetic field lines, Eq. (3) can be written as follows:

$$\frac{\partial N_i}{\partial t} + V_{i\perp} \cdot \nabla N_i = P_i - N_i - \nabla(N_i V_i)_{//} - N_i \cdot \nabla V_{i\perp} \tag{4}$$

where V_i is given by $\mathbf{E} \times \mathbf{B}/B^2$ and V_i includes the effects of plasma diffusion and neutral winds. The set of coefficients for the ion continuity equation is obtained from models of neutral composition, ion and electron temperatures, and production, loss, and diffusion rates as well as $\mathbf{E} \times \mathbf{B}$ drift and neutral wind models (Anderson et al., 1985).

The calculations of the SLIM model are performed based on a modified Chapman function type by modeling some parameters:

$$N_e(h) = N_{max} \exp[c(1 - z - e^{-z})] \tag{5}$$

where

$$z = \frac{h - h_{max}}{A} \tag{6}$$

There are four different coefficients c and A, both for the base (subindex lo) and for the top (subindex top) electron density profiles, that is, c_{Lo}, c_{up}, A_{Lo}, and A_{up}, plus the characteristic peak values $N_{\max}$ and $h_{\max}$.

In summary, six parameters are used to estimate N_e and thus represent the electron density profile in the SLIM model:

N_{max}, h_{max}, c_{Lo}, c_{up}, A_{Lo}, A_{up}

In the SLIM model table, the following ionospheric magnitudes are given:

- The electron density at height h, calculated with the modified Chapman $N_e(h)$.
- The peak maximum electron density $N_{\max}$.
- The peak height of the maximum electron density $h_{\max}$ [km].
- The four coefficients of the modified Chapman function A_{lo}, c_{lo}, A_{up}, and c_{up}.

According to Anderson et al. (1985), these coefficients are suitable for regenerating electron density profiles. These values, as noted previously, are tabulated for each local time in a latitude range from −24° to 24° dip latitude in increments of 4°. The tables are grouped by maximum and minimum solar cycle and within each solar cycle by seasons such as equinox, June solstice, and solstice December, for heights ranging from 180 to 1800 km. The D region contribution can be neglected because the electron density in this region is around one order of magnitude lower than that corresponding to the F region; it also has a relatively small thickness. The TEC plasmaspheric contribution ranges between 2 and 10 TECU and represents almost 50% and 10% of the total electron content for nighttime and daytime conditions, respectively (Roelofs, 1980). Furthermore, when measuring STEC using the Faraday rotation technique, the plasmaspheric contribution can be neglected as this phenomenon is effective below a height of 2000 km. In relation to VTEC comparisons, and given that the height of the GPS satellites' orbit is 20,200 km and that the considered models extend up to about 2000 km in height, an expected fair model prediction would yield $\mathrm{VTEC}_{\mathrm{model}} < \mathrm{VTEC}_{\mathrm{GPS}}$; otherwise, the model prediction would be considered an overestimation.

2. Data and analysis method

2.1. The Tucumán ionospheric model

Considering that most of the satellite–ground ray paths are oblique, *STEC* is the main magnitude to be calculated in order to predict the ionospheric effects on the propagation of radio waves. Accordingly, a model to predict the *STEC* directly has been developed (Scidá, 2013) termed as the "Tucumán ionospheric model" (TIM). It is based on the previous models CHO (Ezquer, 1990) and CHOEA (Cabrera, 2003). In order to improve the TIM performance as a *STEC* predictor in low-latitude and equatorial regions, the modeled values from the IRI model and calculations from the SLIM model have been included. TIM is based on a spatial geometry in which the satellite–receiver path

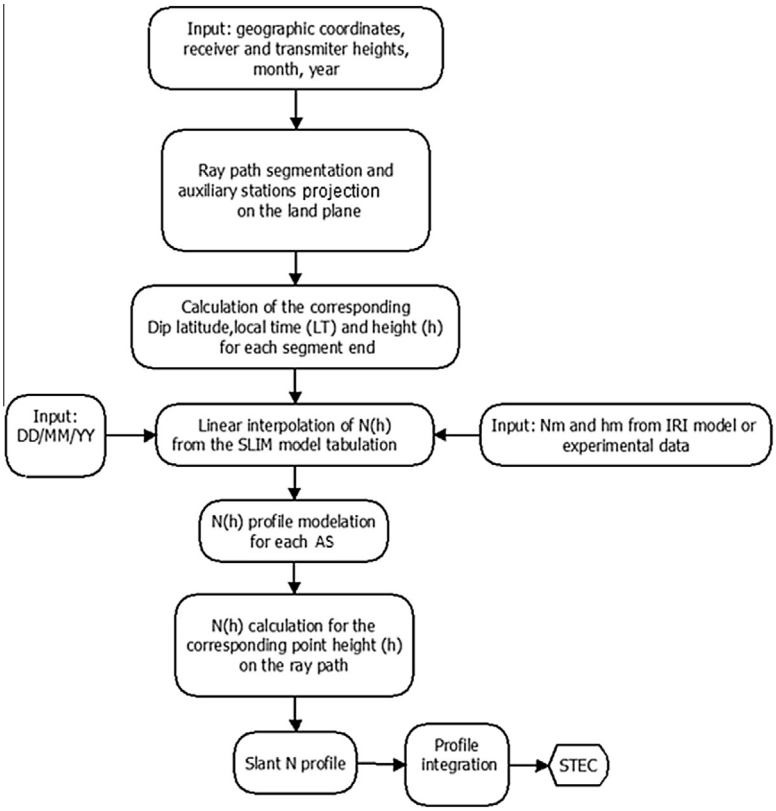

Fig. 2. TIM flowchart.

Table 1
Receiver–GSAT trajectories analyzed for STEC comparisons (the data sources are labeled in the corresponding figure captions).

Trajectory	Rec. Geog. coordinates	Sat. Geog. coordinates
PALEHUA–ATS6	(21.4 N, 201.9 E)	(0, 220 E)
TUCUMÁN–ATS3	(26.9 S, 294.6 E)	(0, 255 E)
LEGON–ATS3	(5.6 N, 359.8 E)	(0, 290 E)
RAJKOT–ETS2	(22.2 N, 70.5 E)	(9.3 N, 130 E)
LUNPING–ETS2	(25.2 N, 122.2 E)	(9.3 N, 130 E)

Table 2
GPS Receiver Stations from the SIRGAS service, used for VTEC comparisons.

Station	Geog. lat.	Geog. long.	Geomag. lat.	Geomag. long.	Dip Lat
MARA (Maracaibo)	10.7	288.3	22.1	358.9	21.64
BOGT (Bogotá)	4.6	285.9	16.5	355.5	16.23
RIOP (Riobamba)	−1.6	281.3	9.7	351.0	10.40
AREQ (Arequipa)	−16.4	288.5	−5.0	358.4	−3.58
TUCU (Tucumán)	−26.8	294.7	−15.5	4.1	−13.34
SANT (Santiago)	−33.1	289.3	−21.7	359.2	−18.00

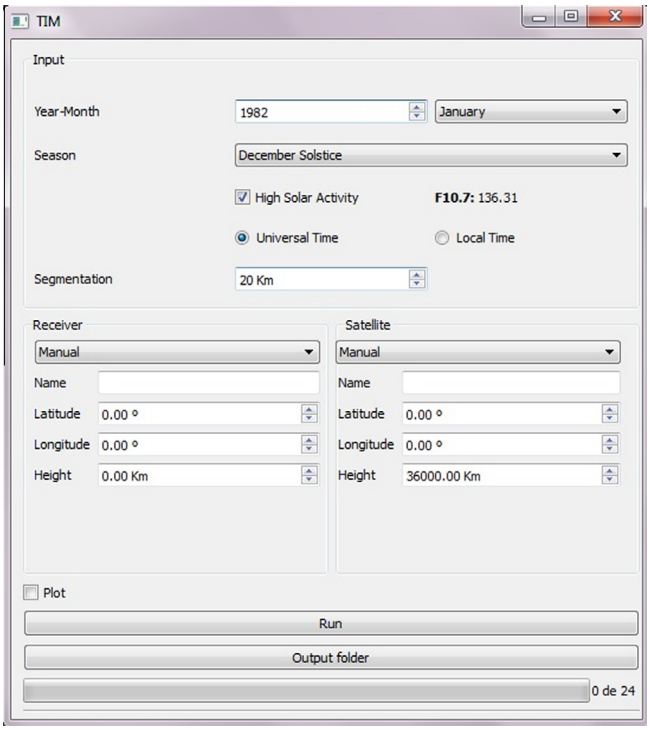

Fig. 3. TIM desktop view (Appendix).

is segmented into sections of 20 km and the projections of those points on the ground form the set of auxiliary stations (ASs).

The electron density of each AS at the corresponding height on the ray path is calculated using the SLIM model; finally, the electron densities of the points on the ray path are integrated to calculate the *STEC*. Fig. 2 shows the flowchart of TIM where the inputs and main calculations are indicated (a view of the model's desktop is shown in Fig. 3 in the Appendix).

The electron densities over the AS, for the coordinates not included in the SLIM table, are calculated by assuming a linear interpolation of the electron density from the four neighboring coordinates, at the corresponding height. This assumption can be considered a good approximation to the real electron density profile, taking into account the quasi-linear variation of this magnitude, in a 4° dip latitude grid, as shown in Fig. 12 in the Appendix.

The SLIM model data tables are modified and converted in spreadsheet programs to allow different input sources for the *STEC* determination. The dip latitude is also calculated by the TIM from a database plus a linear annual variation model of the magnetic dip.

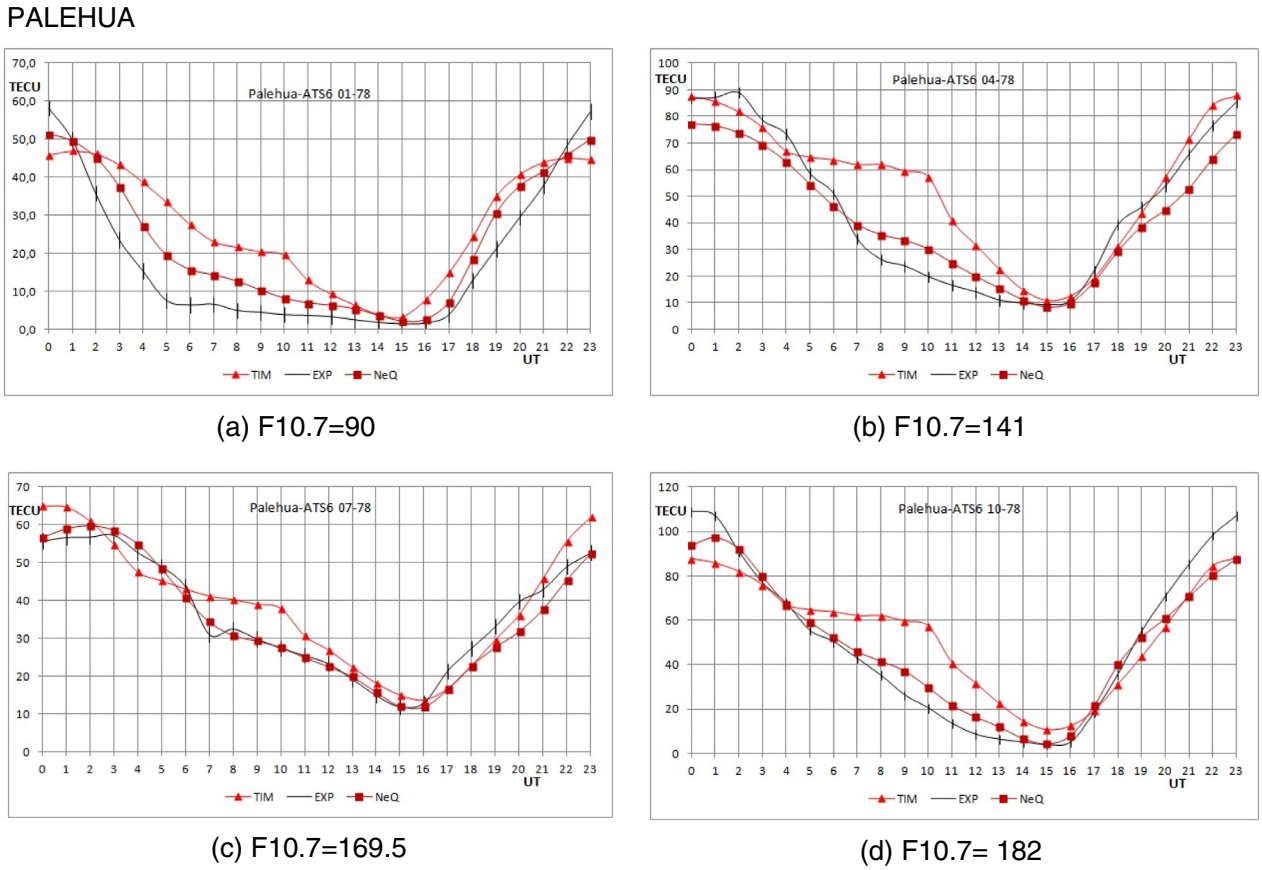

Fig. 4. Modeled and experimental monthly median values of STEC for the Palehua–ATS6 path during equinox (b), (d) and solstice (a), (c) for 1978 (Roelofs, 1980).

2.2. STEC model calculations

In order to evaluate the capacity of TIM to predict STEC, comparisons with experimental data determined by Faraday rotation from GSAT signals were performed. These measurements from GSAT signals are based on the rotation of the polarization plane of the satellite's radio wave due to the interaction of the signal's electric field with the free electrons when it crosses the ionizated plasma, a phenomenon known as Faraday rotation .The STEC is determined from Faraday rotation by (Davies, 1980)

$$\mathrm{STEC} = \frac{f^2}{K_f \cdot M_{400}} (\Omega_F - \Omega_0 - n\pi) \quad (7)$$

where f: radio beacon frequency; K_f: 2.363 constant in SI units; $M_{400} = B{\cdot}\cos\theta$ is the component of the magnetic flux in the ray path direction at a height of 400 km (θ is the angle between B and the ray path); Ω_f: Faraday rotation angle in radians; Ω_0: Initial angle of the polarization plane of the antenna.

Further details are available in the study by Davies (1980).

The predictions were compared with NeQuick calculations (Radicella and Leitinger, 2001). The geographic coordinates of the corresponding trajectories used for STEC studies are shown in Table 1. The data references are labeled in the corresponding figure caption. The following acronyms are used in this work: experimental data, Exp; NeQuick model, NeQ; and TIM model, TIM.

2.3. VTEC model calculations

The *VTEC* can be considered a special case of *STEC* where the elevation angle is 90°. In order to test the performance of TIM in calculating *VTEC*, the model results were compared with the measurement data obtained from GPS signals from the Geocentric Reference System for the Americas (SIRGAS) for 1999, a year with high solar activity. Another study was conducted to evaluate the TIM performance compared with the IRI and NeQuick model predictions.

Table 2 shows the GPS stations considered with their corresponding geographic and magnetic coordinates, and dip latitude.

The VTEC calculations were obtained using the "La Plata ionospheric model" (Brunini et al., 2001). The sampling rate of observation was 30 s and the elevation cutoff mask was set to 20°. To reduce errors due to the obliquity factor, only observations with a zenithal distance lower than 25° were considered. All data were processed daily and then an hourly median VTEC was computed for every station. The data are further explained by Ezquer et al. (2004).

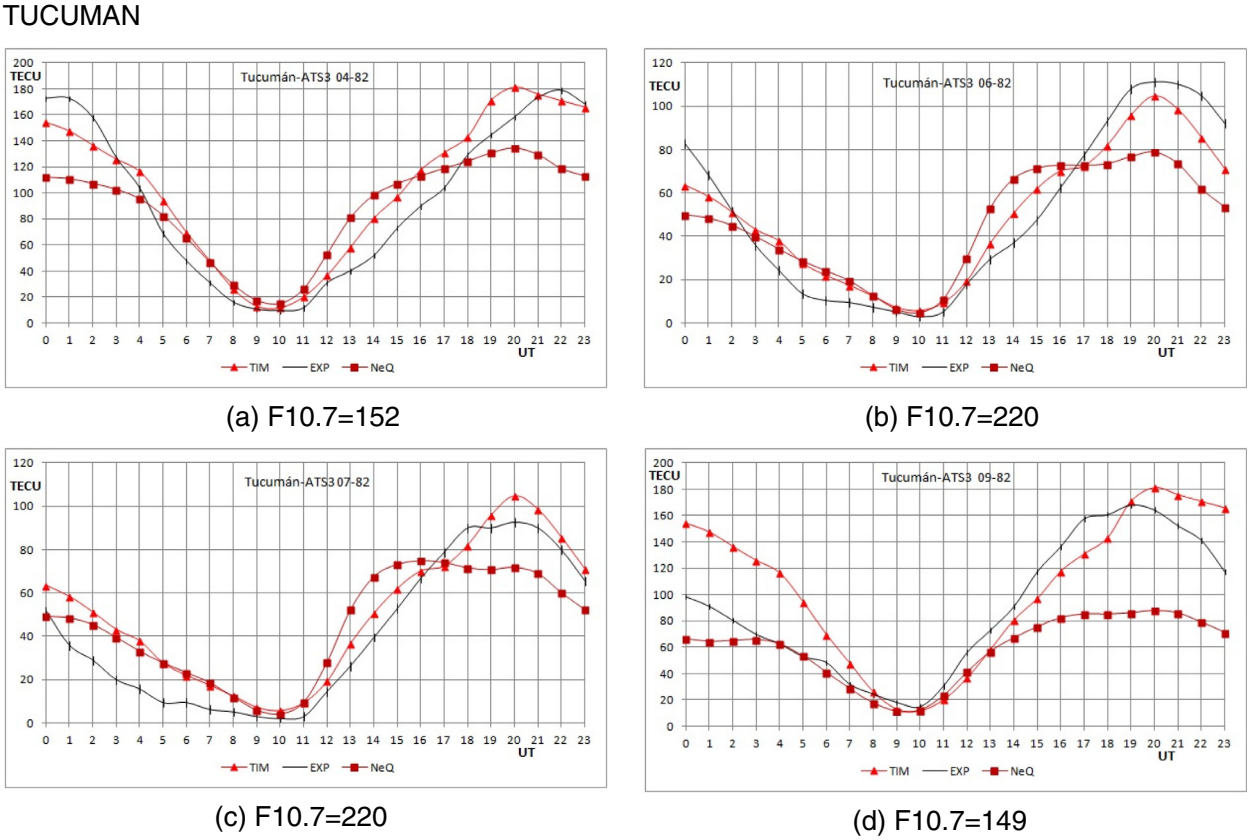

Fig. 5. Modeled and experimental monthly median values of STEC for the Tucumán–ATS3 path during equinox (a), (d) and solstice (b), (c) for 1982, (Tucumán Ionospheric Station, UNT, 1982).

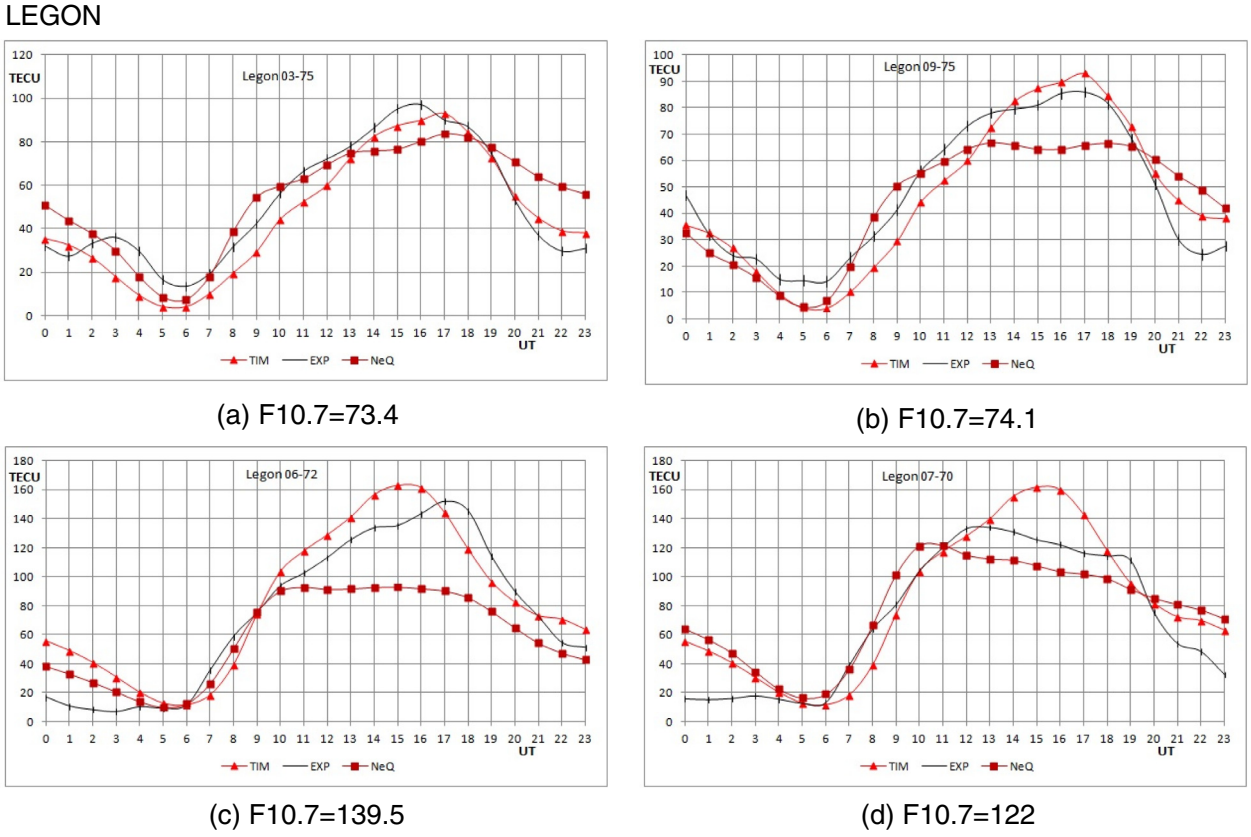

Fig. 6. Modeled and experimental monthly median values of STEC for the Legon–ATS3 path during equinox (a), (b) and solstice (c), (d) for different years (Koster and Beer, 1975).

3. Results and discussion

3.1. STEC calculations

Note: The following acronyms are used in this section for satellites: Application Technology Satellite (ATS) and Engineering Test Satellite (ETS). The studied trajectories are shown in Fig. 9.

3.1.1. ATS6–Palehua

Fig. 4 presents the *STEC* data obtained from geosynchronous satellite signals versus TIM and NeQuick models, for the ATS6–Palehua ray path during the equinox and solstice for 1978 ($F_{10.7} \cong 135$). The TIM reproduces the *STEC* values better during daytime than in the nighttime. The most significant discrepancy to the experimental STEC is observed for the March equinox in Fig. 4b, particularly between 0500 and 1200 UT, where the deviations are close to 40 TECU. For the remaining seasons, the deviation pattern is similar but less pronounced. For the June solstice, Fig. 4c shows the better *STEC* prediction of the TIM, showing errors around 10 TECU. The TIM shows greater deviations than the NeQuick model for almost all hours.

3.1.2. ATS3–Tucumán

Fig. 5 shows the modeled and experimental STEC for the trajectory ATS3–Tucumán for different seasons in 1982. Fig. 5(a)–(c) represent the *STEC* variation during the equinox well, with overall discrepancies <20 TECU. For the September equinox, Fig. 5(d) shows some disagreements during nighttime and before sunrise (10:00 UT) closer to 50 TECU, and a better fitting for the remaining hours. Compared with the NeQuick model, TIM calculations show less deviation to the experimental data for all seasons, except for nighttime and pre-sunrise hours during the September equinox.

3.1.3. ATS 3–Legon

Fig. 6 shows the daily variation in the experimental and modeled *STEC* for the trajectory ATS3–Legon for different seasons and solar activities. In the top panel of Fig. 6 (a) and (b) for the equinox and low solar activity, the TIM predictions show a good reproduction of the STEC satellite data where the disagreements are <10 TECU, in both cases.

In the left bottom panel, for the solstice and high solar activity, Fig. 6(c) show an overall fair fitting to the experimental data with some important deviations before sunrise (from 00:00 to 04:00 UT) and less overestimation in hours of high ionization. The right panel, for the solstice and a slightly higher solar activity, shows more important deviations reaching 40 TECU both for nighttime and around the maximum ionization hours. Compared with the NeQuick model, TIM, in general, gives us more accurate values and a better fitting to the experimental data shape, particularly for maximum ionization hours.

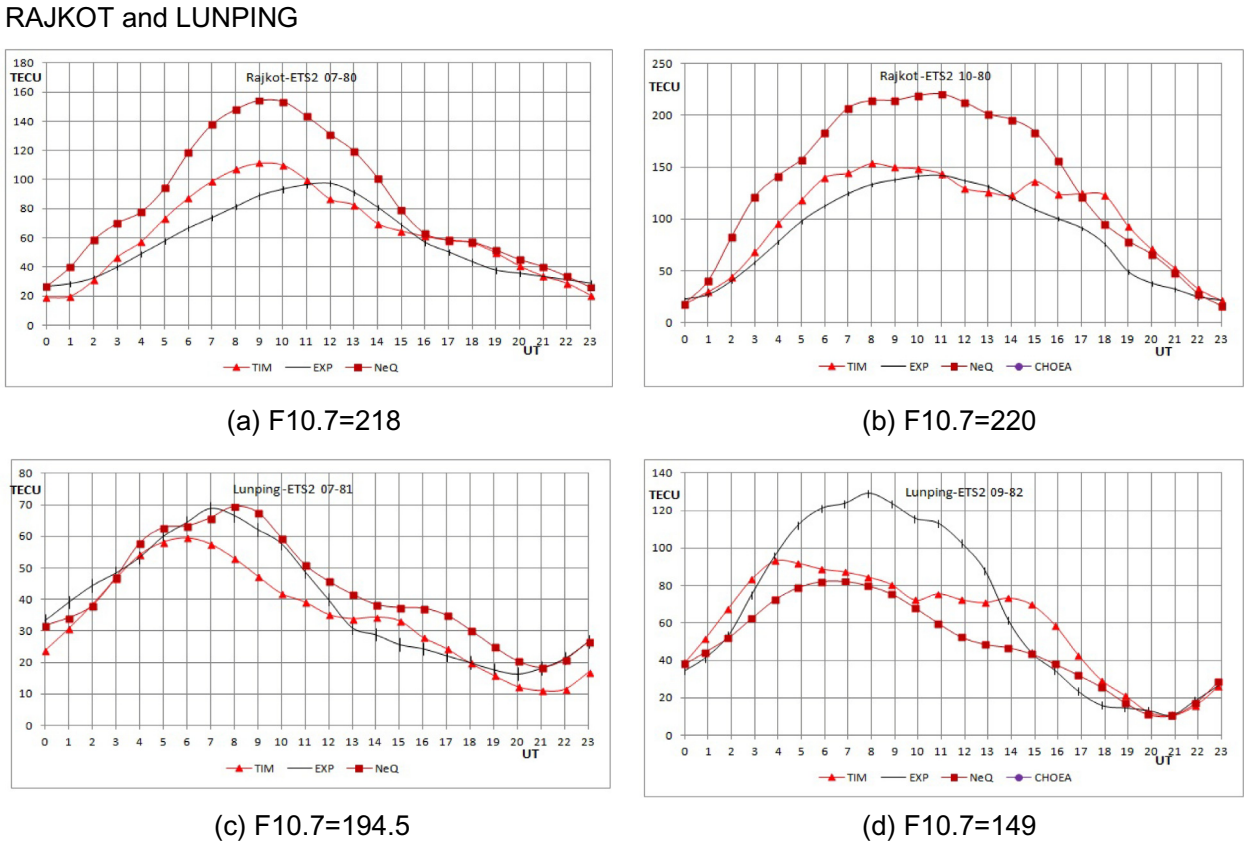

Fig. 7. Modeled and experimental monthly median values of STEC for: (a), (b) Rajkot–ETS2 path (Iyer et al., 1996) and (c), (d) Lunping–ETS2 path (Namara, 1984), for different seasons and years.

3.1.4. ETS2–Rajkot, ETS2–Lunping

For the Asian sector, Fig. 7(a) shows the predictions and measurements for the ETS–Rajkot pathway for the solstice and high solar activity. The TIM shows reasonable fitting to the satellite measurements, giving deviations <20 TECU around the maximum ionization hours. For the equinox and high solar activity, Fig. 7(b) shows a similar fitting to the experimental data. However, in this case, the major disagreements are in the afternoon, reaching values up to 50 TECU. Compared to NeQuick model predictions, it can be clearly seen that TIM shows a better fitting almost for all hours with less absolute deviations.

Fig. 7(c) illustrates the observed and calculated *STEC* for the ETS2–Lunping trajectory for the solstice on solar maximum. No major discrepancy is seen between the TIM predictions and the observed values for the early morning hours from 01:00 to 06:00UT and after sunset from 12:00 to 23:00 UT. Greater deviations are found around the ionization maximum hours from 07:00 to 12:00 UT, when the discrepancies are close to 20 TECU. The TIM predictions underestimate the measured data around the ionization maximum, whereas NeQuick calculates *STEC* more accurately. The situation is reversed in nighttime, from 13:00 to 19:00 UT, where TIM reproduces the experimental data better than NeQuick. Thus, we conclude that both models show, in general, similar deviations. For the equinox at high solar activity, Fig. 7 (d) shows a strong deviation from noon to before sunset (04:00 to 12:00 UT) and a fair fitting for the remaining hours. The TIM predictions show less deviation than NeQuick from early morning to noon (21:00 to 04:00 UT).

3.2. VTEC calculations

Fig. 8 shows the IRI and NeQuick *VTEC* calculations and experimental *VTEC* data for the stations described earlier, for the solstice and equinox in 1999.

For MARA, in June, Fig. 8(a) shows a good fitting of the model's predictions to the measured values during nighttime, with deviations <2 TECU. After 05:00 LT, the discrepancies increase reaching sub-estimations as large as 10 TECU around the maximum hours. Overall, the TIM calculations are superior to the IRI and NeQuick models for almost the entire day, particularly during the night. For the equinox, as seen in Fig. 8(b), the deviations in nighttime are greater than those observed during the solstice, with similar sub-estimations during the day and a slight overestimation at maximum hours (from 12:00 to 15:00 LT). These large deviations from experimental data could be interpreted considering the proximity of the

Fig. 8. Modeled and experimental monthly median values of VTEC for: (a) and (b) Maracaibo; (c) and (d) Bogota; (e) and (f) Riobamba; (g) and (h) Arequipa; (i) and (j) Tucumán; (k) and (l) Santiago, during solstice and equinox for 1999 ($F10.7 \approx 160$).

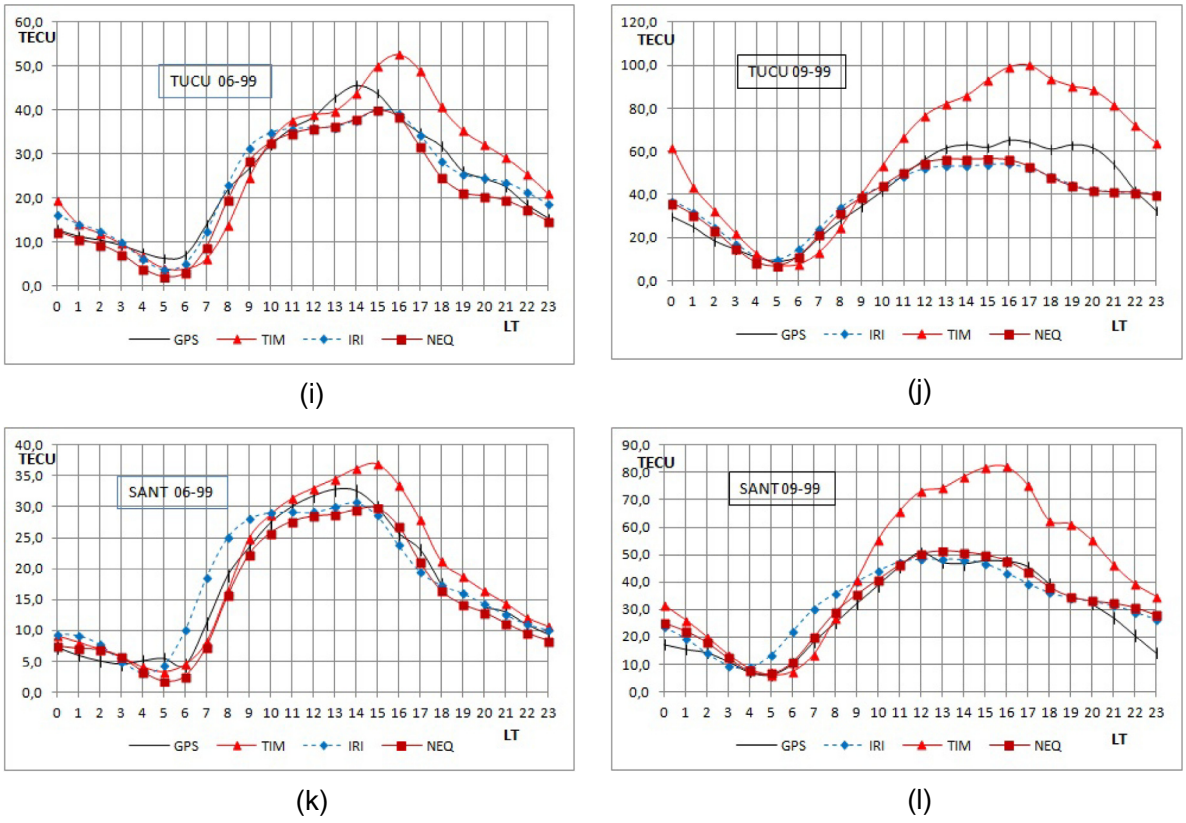

Fig 8. *(continued)*

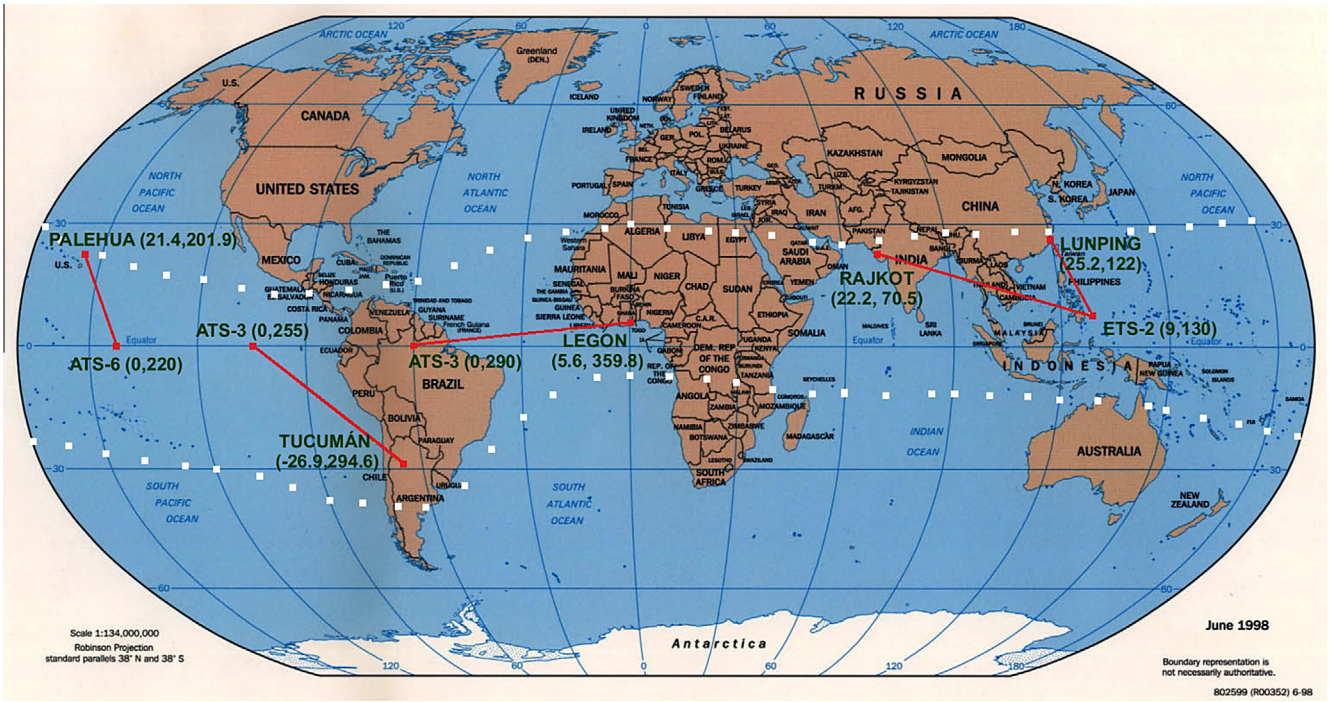

Fig. 9. Slant TEC trajectories analyzed in red lines, and isoclines +24 to −24 lat dip in white spots (limits of validity of the TIM). (For interpretation of the references to color in this figure legend, the reader is referred to the web version of this article.)

Table 3
Distribution of the deviations of the STEC relative model: green (dark grey) 0–30% (57% cases); yellow (light grey) 31–50% (16% cases); red (grey) >51% (27% cases).

STEC	Palehua (21.4, 201.1)				Tucumán (-26.8, 294.7)						Legon (5.6 , 359.8)											Rajkot (22.2; 70.5)		Lunping (25.2; 122.2)
Date:	1978/1	1978/4	1978/7	1978/10	1982/4	1982/5	1982/6	1982/7	1982/8	1982/9	1969/4	1969/12	1970/7	1972/3	1972/6	1972/9	1972/12	1975/3	1975/6	1975/9	1975/12	1981/7	1981/10	1981/7
F10.7:	89,61	141,41	169,51	182,01	152,21	132,11	235,81	274,01	173,01	149,01	181,21	135,91	121,91	135,31	139,51	103,41	116,1	73,4	68,9	74,1	71,8	194,51	287,12	194,51
0 LT	252	20	20	205	12	104	56	141	380	87	74	1	257	145	231	108	-10	11	12	-24	-42	-5	77	43
1	181	15	15	270	37	135	105	194	463	79	147	-13	224	125	357	154	16	18	1	1	-34	-24	72	19
2	158	16	16	254	46	164	112	133	508	45	88	-9	157	145	400	136	48	-20	31	11	-46	-38	49	4
3	117	21	21	188	56	223	85	180	405	51	140	2	74	129	346	185	36	-50	47	-21	-50	-49	19	-5
4	133	25	25	176	65	129	72	143	258	8	84	58	34	55	100	108	40	-68	48	-38	-51	-39	-6	-24
5	369	5	5	148	24	94	41	140	151	-27	54	145	4	-9	40	13	-10	-75	-28	-71	-67	-30	-6	-38
6	288	-22	-22	4	25	128	90	193	159	-19	-9	198	-9	5	3	7	41	-70	-70	-71	-39	-20	28	-49
7	89	-17	-17	-13	75	114	81	208	114	-34	-18	95	-52	9	-47	8	6	-47	-70	-56	-32	-12	29	-39
8	65	-11	-11	-21	20	84	8	32	23	-34	-20	22	-38	5	-33	36	-7	-38	-52	-38	-29	-1	31	-30
9	38	-9	-9	-19	46	90	25	39	30	-20	-13	21	-8	26	-1	51	-6	-31	-33	-29	-32	6	32	-20
10	16	7	7	-16	56	112	37	28	21	-11	-2	17	0	24	11	57	6	-21	-6	-21	-32	2	29	-12
11	-7	14	14	-14	33	91	30	18	3	-17	14	15	-2	29	15	61	17	-21	-1	-18	-24	-1	29	-1
12	-22	18	18	-18	31	77	12	5	2	-14	30	25	-4	32	14	71	35	-17	-2	-18	-14	-9	18	6
13	-21	17	17	-20	26	53	-6	-8	6	-17	40	27	4	32	13	73	36	-7	-20	-7	-13	-13	15	2
14	-6	14	14	-20	11	35	-12	-9	7	-11	43	13	19	30	17	86	32	-5	-17	4	5	-15	9	-1
15	29	7	7	-10	18	40	-11	7	26	2	53	11	29	33	21	92	37	-8	-12	8	18	-20	5	-9
16	84	-4	-4	-1	15	38	-6	13	40	10	60	23	31	33	13	99	31	-8	-20	5	16	-12	0	-13
17	152	-10	-10	-1	2	36	-10	10	47	15	55	33	23	27	-5	107	31	3	-28	8	16	-7	-7	-15
18	339	-8	-8	17	-5	35	-18	7	63	21	45	39	3	26	-18	102	53	-3	-43	3	9	12	-3	-20
19	327	-1	-1	27	-1	40	-23	9	98	41	104	53	-14	60	-15	109	67	-3	-51	6	8	25	6	-12
20	247	32	32	45	-11	34	-23	23	118	57	134	69	9	163	-8	132	34	4	-32	8	10	35	23	-7
21	336	24	24	77	-15	36	-14	63	168	62	102	46	34	242	1	107	-6	21	2	49	-12	43	25	12
22	355	30	30	127	-13	43	-1	77	200	70	68	47	45	355	30	103	-10	32	26	59	-31	19	36	25
23	408	38	38	181	-1	63	21	116	286	81	98	23	95	257	25	107	-12	23	14	38	-45	4	64	35

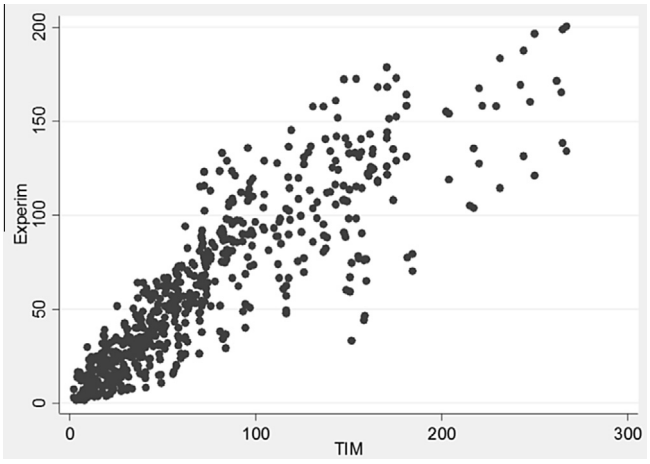

Fig. 10. Scatterplot of Experim versus TIM for all cases.

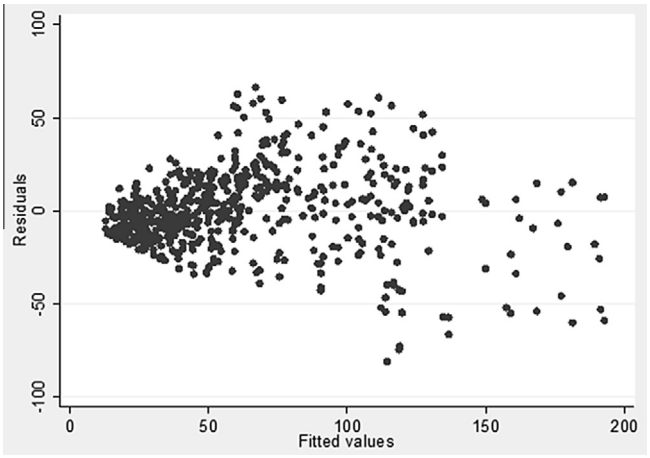

Fig. 11. Scatterplot of residuals versus fitted values for all cases.

station BOGT (Geomag. lat 16.5°) to the north peak of the EA, located approximately 15° geomagnetic. Thus, the model's calculation underestimates the contribution of the plasma fountain effect (Martyn, 1947).

Fig. 8(c) shows the monthly median of VTEC for the BOGT station, for the June solstice. A good reproduction of the experimental values from sunset until dawn is observed. Since then (06:00 LT) and for the rest of the daylight hours, the model underestimates with errors close to 25 TECU (from 11:00 to 13:00 LT). Later, the deviations decrease closer to sunset. All of the model's calculations are close to each other for all hours, showing similar considerable errors from 06:00 to 18:00 LT. For the equinox, Fig. 8 (d) shows a good reproduction of the experimental values from 05:00 to 10:00 LT. Around noontime, some overestimations with errors reaching up to 20 TECU close to the maximum ionization hours can be observed. In nighttime, the TIM deviations are greater than those of the other two models. These situation is reversed during the day, from 10:00 LT to sunset, where TIM shows less deviations from

Table 4
Sample size, *p*-value, and *R*-squared for TIM, NeQuick, and IRI models.

Data	*N*	*p*-value	R^2
TIM	876	<0.0001	0.77
NEQ	876	<0.0001	0.72
IRI	276	<0.0001	0.82

the experimental data than IRI and NeQuick. Fig. 8(e) shows the hourly monthly median of VTEC for the RIOP station for the solstice. The experimental values from the afternoon until sunrise hours (17:00 to 06:00 LT) are well reproduced. Around noontime and up until sunset (11:00 to 20:00 LT), the model underestimates, showing errors close to 30 TECU. Overall, the TIM predictions are better than those of IRI and NeQuick for all hours. For the equinox, Fig. 8(f) shows that the model overestimates during the late evening and in nighttime (from 18:00 to 04:00 LT) reaching up to 50 TECU at 00:00 LT. During daytime hours, the model results are fitted to the experimental data shape with absolute errors close to 10 TECU. Compared with the IRI and NeQuick, the TIM results are better during all daylight hours. For the RIOP station, during the solstice, Fig. 8(e) shows a good agreement in nighttime and before sunrise and underestimations during daylight hours with absolute errors <20 TECU. For the equinox in Fig. 8(f), the opposite is observed: considerable disagreements in nighttime and a better fitting from 05:00 to 18:00LT with overall underestimations close to 10 TECU. For both the solstice and equinox, TIM shows better predictions than IRI and NeQuick. For the AREQ station during the solstice, we find an overall good fitting with some underestimations <10 TECU from 06:00 to 13:00 LT and similar overestimations for the remaining hours of the day.

For the TUCU station, during the solstice, Fig. 8(i) shows a good fitting to experimental data since 00:00 to 14:00 LT with deviations < 10 TECU, increasing close to the maximum hours and later with errors around 15 TECU. Moreover, the shape of the hourly experimental data is again well represented by the TIM. From 00:00 LT to 15:00 LT, the TIM predictions are similar to those calculated by the IRI and NeQuick models, except for a few hours in the afternoon, starting at 16:00 LT, where the TIM overestimates.

During the equinox, Fig. 8(j) shows that the model overestimates for almost all hours, with deviations reaching values close to 40 TECU at maximum ionization. Minor deviations are observed for predawn hours and until 10:00 LT with errors close to 5 TECU. Compared with IRI and NeQuick, the TIM, in this case, shows larger deviations from 10:00 LT to nearly sunrise.

For the SANT station, during the solstice, Fig. 8(k) shows a good agreement with experimental data, with overestimations close to 10 TECU around the maximum ionization hours and less deviations in nighttime. In this case, IRI and NeQuick give more accurate predictions for all hours.

For the equinox, a similar situation can be observed in Fig. 8(l) with greater deviations for almost all hours.

3.3. Model deviations

Table 3 summarizes the model relative percentage deviations calculated by

$$\Delta\% = (STEC_{TIM} - STEC_{Exp})/STEC_{Exp} \times 100 \quad (8)$$

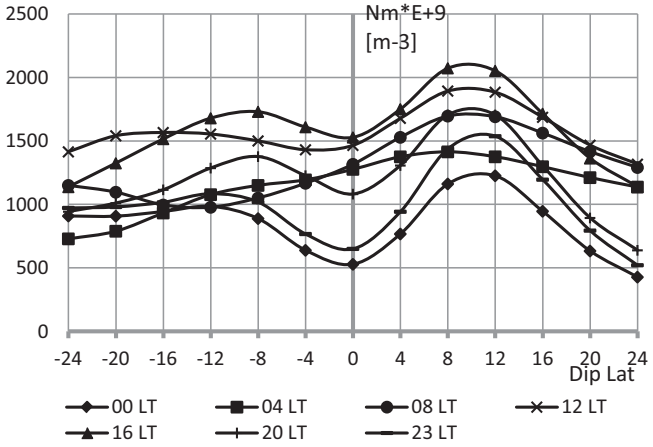

Fig. 12. Latitudinal variation of the maximum electron density (Nm) during solstice and high solar activity (December).

They are presented in three ranges: 0–30%, 31–50%, and >50%. It can be observed that the minor deviations, from 0% to 30%, are located in the center of the table and represent 57% of the cases studied. In the next range, 31–50%, the deviations are slightly scattered, accounting for 16% of the cases. Finally, the range >50% represents 27% of the full cases; these deviations are primarily located close to the post-sunset and pre-sunrise hours, and during nighttime.

Minor deviations are found for moderate and low solar activity, that is, Legon 1972/12, 1975/03/06/09/12, except for Palehua 1978/01.

The model's deviations observed for VTEC are very similar to those for STEC, showing slightly better results in general. Here, the range for deviations <30% is 60% of the studied cases; the calculations with errors in the range between 30% and 50% are around 18% of the analyzed cases; and the worst predictions, that is, deviations >50%, account for 22% of the cases.

3.4. Statistical analysis of the model

We conduct a statistical analysis to assess the predictive power of the TIM. The aim of this analysis is to determine whether the values predicted by TIM describe the experimental data sufficiently well. Fig. 10 displays a scatterplot of the full sample of observed data (Experim) against the TIM values. To evaluate how well the model follows the observed experimental data, we fit a linear regression line using the ordinary least squares (OLS). The results show that the model is statistically significant ($R^2 = 0.76$ and p-value < 0.0001). More specifically, the TIM explains 76% of Experim variability. A scatterplot of the residuals is shown in Fig. 11. It can be observed that about 97.5% of the residues calculated after adjustment are between −50 and 50, and only 2% of the residuals are greater. These larger deviations could be caused by the nighttime and pre-sunrise significant model errors mentioned previously. Similar analyses were performed for NeQuick and IRI models, and the results are gathered in Table 4. In both

OLS regressions, TIM is statistically significant, with high *R*-squared and low *p*-values. In comparison to NeQuick, TIM shows a slightly better fitting to measured data.

In summary, the results suggest that we cannot reject the TIM as a STEC calculator.

4. Conclusions

A model for *STEC* predictions in low-latitude and equatorial regions, the TIM, has been developed. It is used to calculate the *STEC* between any two points in space, or between a ground station and a point in space for low-latitude and equatorial regions. In terms of the performance of all models, the TIM is most appropriate for STEC calculations in equatorial and low-latitude regions. This is mainly because the model's calculation structure takes into account the features of the low-latitude electrodynamics in the ionosphere, and the effect of the horizontal gradients.

The main contributions of the TIM can be summarized as follows:

- It calculates *STEC* directly without using VTEC and mapping functions for any spatial configuration ray path.
- It improves the accuracy of satellite positioning systems.
- It improves the accuracy of the *STEC–VTEC* mapping functions.
- It enhances the piercing-point height modeling.
- Other ionospheric magnitudes such as *NmF2, hmF2*, elevation and azimuth angles for a given spatial trajectory, magnetic dip, dip latitude, and solar flux F10.7 can be obtained by a "click" from the model calculations.

The model has been tested in different satellite-to-ground trajectories worldwide by comparing its calculations to direct measurements obtained by Faraday rotation techniques using GSAT signals, and GPS data for VTEC comparisons.

The results show that the model performs better during daytime than in nighttime for most of the studied cases.

In general, a good approximation of the model calculations to the experimental values is observed, which generally follows the shape of the hourly variation of the monthly STEC median, where 57% of the values show deviations <30%.

Furthermore, the inspection of the residuals supports the validity of the model. Similar conclusions were obtained when a separate OLS analysis was conducted for high and low solar activity.

In some cases, different deviations can be observed for the March equinox (EM) from those for the September equinox (ES), which can be attributed to the effects of the equinoctial asymmetry. A similar interpretation based on the annual anomaly can be applied to understand the differences between the model errors for June and December solstices for a considered year.

For VTEC calculations, the model reproduces the measured data showing similar deviations to those described for *STEC* predictions, that is, almost 60% of cases being <30% and 18% of cases ranging between 31% and 50%. Only the remaining 22% of the studied cases have shown deviations >51%. Overall, the model's deviations increase from north to south.

Compared with the NeQuick model, the TIM better reproduces the *STEC* hourly profile shape, showing more suitable results. Due to this, the slant trajectories cross the EIA structures with different elevations and azimuth angles; the model discrepancies also differ, as expected. However, a better fit is observed during the solstices than on equinoxes, and even better estimations for low than for high solar activity. Nevertheless, the TIM fairly reproduces the *STEC* measured data with disagreements <30% almost for 60% of the studied cases. Considering some important deviations observed during nighttime, these calculations must be improved by studying the anomalies caused by the electrodynamics, the recombination, and transport processes carried out after sunset and before sunrise hours. The most important nighttime processes are as follows: (a) the well-known vertical drift driven by the zonal electric field in the F region, generated by the polarization phenomena developed due to the thermospheric wind and the sharp gradients in the E region (Abdu, 2005); (b) the neutral winds due to pressure gradients, leading to vertical currents and polarization fields on both sides of the solar terminator (Rishbeth, 1971; Farley, 1959); and (c) the sudden downward excursion in the vertical plasma drift around local sunrise time followed by an upward turning, observed in the equatorial ionosphere (Prabhakaran Nayar et al., 2009).

Future research should aim at improving the TIM calculations by modeling the coefficients used in the modified Chapman equation, particularly for nighttime, to obtain more accurate *STEC* predictions.

Acknowledgments

This research is supported by projects PICT2011-1008 (FONCyT-MINCyT-Argentine), PIUNT26/508 Universidad Nacional de Tucuman (Argentine), PIP 0611 CONICET, and PID 25/P047 Universidad Tecnológica Nacional.

The authors thank their colleagues at ARPL/ICTP for making the web version of the NeQuick model available.

Appendix A

Fig. 3 shows the TIM desktop view. The data inputs are year, month, UT or LT, geographic coordinates and height of the two ends of the trajectory, and segmentation length. The model's output gives us F10.7 solar flux, local time (or universal time), *STEC* values between the mentioned points, and *STEC* versus LT or UT plot as an option. It also allows the user to record the coordinates and height of the two points and their corresponding name.

References

Abdu, M.A., 2005. Equatorial ionosphere-thermosphere system: electrodynamics and irregularities. Adv. Space Res. 35 (5), 771–787.

Anderson, D.N., Mendillo, M., Herniter, B., 1985. A Semi-Empirical Low Latitude Model, Project 2310. Air Force Geophysics Laboratory, USA.

Appleton, E.V., 1946. Two anomalies in the ionosphere. Nature 175, 691.

Berkner, L.V., Wells, H.V., Seaton, S.L., 1936. Characteristics of the upper region of the ionosphere. Terrest. Magn. Atmos. Electron. 41, 173–184.

Bilitza, D., Reinisch, B.W., 2008. International reference ionosphere 2007: improvements and new parameters. Adv. Space Res. 42 (4), 599–609.

Brunini, C., Meza, A., Diaz, A., 2001. Regional vertical total electron content using GPS observation. IAG Scientific Assembly.

Cabrera, M.A., 2003. Modelado de la distribución electrónica en la ionósfera - Modelado del contenido electrónico total oblicuo (Ph.D. dissertation). Universidad Nacional de Tucumán.

Cesaroni, C., Spogli, L., Alfonsi, L., De Franceschi, G., Ciraolo, L., et al., 2015. L-band scintillations and calibrated total electron content gradients over Brazil during the last solar maximum. J. Space Weather Space Clim. 5, A36.

Chapman, S., 1931. The absorption and dissociative or ionizing effect of monochromatic radiation in the atmosphere on a rotating earth. Proc. Phys. Soc. London 43, 26.

Das Gupta, A., Paul, A., Ray, S., 2002. Ionospheric Total Electron Content and WAAS in the Indian Zone. Institute of Radio Physics and Elec., University of Calcutta.

Davies, K., 1980. Recent progress in satellite radio beacon studies with particular emphasis on the ATS-6 radio beacon experiment. Space Sci. Rev. 25, 357–430.

Duncan, R.A., 1960. The equatorial F-region of the ionosphere. J. Atmos. Terrest. Phys. 18, 89–100.

Ezquer, R.G., 1990. Estudio del comportamiento del contenido electrónico ionosférico sobre Tucumán. Su modelado a partir de ionosondas (Tesis Doctoral). Facultad de Ciencias Exactas y Tecnología, Universidad Nacional de Tucumán.

Ezquer, R., Brunini, C., Mosert, M., Meza, A., Oviedo, R., Kiorcheff, E., Radicella, S., 2004. GPS-VTEC measurements and IRI predictions in the South American sector. Adv. Space Res. 34 (9), 2035–2043.

Farley Jr., D.T., 1959. A theory of electrostatic fields in a horizontally stratified ionosphere subject to a vertical magnetic field. J. Geophys. Res. 64, 1225–1234.

Gulyaeva, T.L., 1999. Regional analytical model of ionospheric total electron content: monthly mean and standard deviation. Radio Sci. 34 (6), 1507–1512.

Hanbaba, R., Zolesi, B., 2000. Improved quality of service in ionospheric telecommunication systems planning and operation: COST 251 major achievements. Física de la Tierra 12 (61–10).

Iyer, K.N., Joshi, H.P., Jivrajani, R.D., Aravindakshan, P., 1996. Comparative study of STEC near the crest of the equatorial anomaly with IRI model for solar minimum to solar maximum. Adv. Space Res. 18 (6), 233–236.

Komjathy, A., 1997. Global ionospheric total electron content mapping using the global positioning system (Ph.D. dissertation). Dep. Of Geod. And Geomatics Eng., Univ. of New Brunswick, Fredericton, N.B., Canadá.

Koster, J.R., Beer, T., 1975. Study of the Equatorial Anomaly, Interim Report No. 2. Dep. of Physics, University of Ghana, Legon, Ghana.

Martyn, D.F., 1947. Atmospheric tides in the ionosphere. I. Solar tides in the F2 region. Proc. Roy. Soc. (London) A189, 241–260.

Migoye Orue, Y., Nava, B., Radicella, S., Alazo-Cuartas, K., 2015. GNSS derived TEC data ingestion into IRI 2012. Adv. Space Res. 55 (8, 15), 1994–2002.

Namara, L.F., 1984. Prediction of total electron content using the International Reference Ionosphere. Adv. Space Res. 4 (1), 25–50.

Panda, S.K., Gedam, S.S., Rajaram, G., 2015. Study of ionospheric TEC from GPS observations and comparisons with IRI and SPIM model predictions in the low latitude anomaly Indian subcontinental region. Adv. Space Res. 55 (8), 1948–1964.

Prabhakaran Nayar, S.R., Mathew, T.J., Sreehari, C.V., Sumod, S.G., Devasia, C.V., Ravindran, S., Sreeja, V., Kumar Pant, T., Sridharan, R., 2009. Electrodynamics of the equatorial F-region ionosphere during pre-sunrise period. Ann. Geophys. 27, 107–111.

Radicella, S.M., Leitinger, R., 2001. The evolution of the DGR approach to model electron density profiles. Adv. Space Res. 27, 35–40.

Reinisch, B.W., 2000. Radio Sounding of Geospace Plasmas, Física de la Tierra, 12. Servicio de Publicaciones, Universidad Complutense, Madrid, pp. 105–126.

Rishbeth, H., 1971. Polarization fields produced by winds in the equatorial region. Planet. Space Sci. 19, 357.

Roelofs, T.H., 1980. Plasmapheric, Faraday and total electron contents, 1977 and 1978, report. University of Hawaii, Honolulu, Hawaii. AFGL-TR-81-0143 (final rep.).

Scidá, L.A., 2013. Modelado de la distribución de la densidad de electrones libres entre dos puntos en la ionósfera (Ph.D. dissertation). Departamento de Física, Facultad de Ciencias Exactas y Tecnología, Universidad Nacional de Tucumán, Argentina, p. 208.

Smith, D.A., Araujo Pradere, E.A., Minter, C., Fuller Rowell, T., 2008. A comprehensive evaluation of the errors inherent in the use of a two-dimensional shell for modeling the ionosphere. Radio Sci. 43, RS6008. http://dx.doi.org/10.1029/2007RS003769.

Warnant, R., Jodogne, J.C., 1998. A comparison between the TEC computed using GPS and ionosonde measurements. Acta Geod. Geoph. Hungarica 33 (1), 147–153.